Comparing the Halogen Bond to the Hydrogen Bond by Solid-State NMR Spectroscopy: Anion Coordinated Dimers from 2- and 3-Iodoethynylpyridine Salts

Patrick M. J. Szell,[a] Gabriella Cavallo,[b] Giancarlo Terraneo,[b] Pierangelo Metrangolo,[b] Bulat Gabidullin,[a] and David L. Bryce*[a]

Abstract: Halogen bonding is an increasingly important tool in crystal engineering, and measuring its influence on the local chemical and electronic environment is necessary to fully understand this interaction. Here, we present a system-atic crystallographic and solid-state NMR study of self-complementary halogen-bonded frameworks built from the halide salts (HCl, HBr, HI, HI_3) of 2-iodoethynylpyridine and 3-iodoethynylpyridine. A series of single crystal X-ray struc-tures reveals the formation of discrete charged dimers in the solid state, directed by simultaneous $X^{@}\cdots H@N^{+}$ hydrogen bonds and $C@I\cdots X^{@}$ halogen bonds (X = Cl, Br, I). Each com-pound was studied using multinuclear solid-state magnetic resonance spectroscopy, observing ^{1}H to investigate the hy-drogen bonds and ^{13}C, ^{35}Cl, and $^{79/81}Br$ to investigate the halogen bonds. Anatural localized molecular orbital analysis was employed to help interpret the experimentalresults. 1HSSNMR spectroscopy reveals adecrease in the chemical shift of the proton participating in the hydrogen bond as the halogen increasesinsize, whereas the 13CSSNMRreveals an increased 13Cchemical shift of the C@Icarbon for C@I···X@ relative to C@I···N halogen bonds. Additionally, 35Cl and 79/81Br SSNMR, along with computational results, have allowed us to compare the C@I···X@ halogen bond involving each halide in terms of NMR observables. Due to the isostructural nature of these compounds,they are ideal cases for experimentally assessing the impact of different halogen bond acceptors on the solid-stateNMR response.

Introduction

Supramolecular chemistry has been established as an essential branch of chemistry, with the concept of charge transfer complexes recognized by the Nobel Prize in chemistry in 1969, and the first observations on crown ether complexes leading to the Nobel Prize in chemistry in 1987.[1,2] Alongside supramolecular chemistry, the field of crystal engineering was born, with the intention of designing the structures of solids with specific properties and for particular applications.[3] One of the most important tools in these fields has arguably been the hydrogen bond,[4] which has been extensively explored both in synthetic chemistry as well as in biological systems. Recent developments in the field of non-covalent interactions, including the theoretical aspects of σ-hole and π-hole interactions,[5–7] have offered the crystal engineer many additional tools in their pursuits of novel materials. From these interactions, the tetrel bond,[8] pnictogen bond,[9] chalcogen bond,[10] and halogen bond,[11] named from their electrophilic site,[12] have gained considerable attention.[13] The halogen bond is the most explored of these interactions, owing to its strength and versatility, with authoritative reviews on the subject available.[14,15]

The halogen bond is a non-covalent interaction between the region of positive electrostatic potential along the extension of a covalently bonded halogen, typically called the σ-hole,[16] and a Lewis base. The covalently bonded halogen, named the halogen bond donor (X), interacts with an electron donor, that is, the halogen bond acceptor (Y).[17] The halogen bond has been explored as a versatile interaction alternative to the hydrogen bond,[18] offering a highly linear bond ($\theta_{R-X\cdots Y}$ = 150–180°, where R denotes a covalently bonded substituent).[19–21] The presence of the halogen bond can be further recognized using the normalized distance parameter (R_{XB}), given in Equation (1), which is the quotient of the halogen bond length ($d_{X\cdots Y}$) and the sum of the van der Waals radii of both atoms participating in the halogen bond (d_{vdW}).[22] Thus, $R_{XB} < 1$ indicates the presence of a short contact, with smaller numbers suggesting a stronger halogen bond. If $R_{XB} > 1$, there is no contact to speak of. Halogen bonds are typically charac-

[a] P. M. J. Szell, Dr. B. Gabidullin, Prof. D. L. Bryce
Department of Chemistry and Biomolecular Sciences
University of Ottawa, 10 Marie Curie Private, Ottawa
Ontario, K1N 6N5 (Canada)
E-mail: dbryce@uottawa.ca

[b] Prof. G. Cavallo, Prof. G. Terraneo, Prof. P. Metrangolo
Laboratory of Supramolecular and Bionanomaterials
Department of Chemistry
Materials and Chemical Engineering "Giulio Natta"
Politecnico di Milano
Via L. Mancinelli 7, 20131 Milano (Italy)

Supporting information and the ORCID identification number(s) for the au-thor(s) of this article can be found under: https://doi.org/10.1002/chem.201801279.

terized by R_{XB} values of approximately 0.65 (very strong) to 0.95 (weak).

$$R_{XB} = \frac{d_{X\cdots Y}}{\sum d_{vdW}} \quad (1)$$

The halogen bond is highly tuneable, with the size of the σ-hole increasing with the size of the halogen.[16] The inclusion of electron withdrawing groups on the halogen bond donor moiety, such as fluorine[23,24] or the placement of halogens on ethynyl carbons,[25,26] further increases the magnitude of the σ-hole. For these reasons, the halogen bond is a valuable tool for the crystal engineer,[27,28] and a proper understanding will allow this interaction to be fully exploited.

Solid-state NMR (SSNMR) spectroscopy is a powerful tool to characterize the halogen bond,[29,30] offering insights into both the halogen bond acceptor and the halogen bond donor. The information offered by SSNMR is obtained through various parameters including chemical shifts,[31–33] the quadrupolar coupling tensor,[34–38] dipolar coupling,[39] and *J*-coupling;[38,40] these data are then used to provide structural, electronic, crystallographic, and/or dynamical information.[41] SSNMR experiments on the quadrupolar halides, $^{35/37}$Cl (spin $I = 3/2$), $^{79/81}$Br (spin $I = 3/2$), and ^{127}I (spin $I = 5/2$), have provided direct information on the electric field gradient at the halogen bond acceptor,[34–36] which relates to the local and long-range molecular and crystal structures. The chlorine halogen bond donor has recently been directly probed by ultra-wideline ^{35}Cl SSNMR spectroscopy.[37]

Quadrupolar coupling results from the interaction between the electric field gradient (EFG) at a spin $> {}^1/_2$ nucleus and its electric quadrupole moment (*Q*). This quadrupolar interaction (QI) can be described by a traceless second-rank tensor with three components: $|V_{33}| \geq |V_{22}| \geq |V_{11}|$. The magnitude of the interaction is given by the quadrupolar coupling constant [C_Q, Eq. (2)], and the axial symmetry of the QI tensor is described by the asymmetry parameter [η, Eq. (3)].

$$C_Q = \frac{eV_{33}Q}{h} \quad (2)$$

$$\eta = (V_{11} - V_{22})/V_{33} \quad (3)$$

Despite the growing interest in iodoacetylenes,[42–47] there have been limited SSNMR studies of halogen-bonded compounds built with this functional group.[48–51] Furthermore, there have been no systematic investigations to date comparing the effects of various halogen bond acceptors in isostructural compounds on the SSNMR observables, and no information is available directly comparing the halogen bond to the hydrogen bond in terms of NMR responses. Here, we present the crystal structures for a series of self-complementary frameworks and charged dimers based on the halide salts of 2-iodoethynylpyridine (2-IEP) and 3-iodoethynylpyridine (3-IEP), shown in Figure 1, and investigate them by multinuclear solid-state magnetic resonance. In these examples, the halogen bond donor is the iodine on the acetylene group, whereas the halogen bond acceptor is either the nitrogen on the heterocycle for the neutral compounds, or the halide anions of the salts. The ^{13}C SSNMR spectra of these compounds allows us to compare the effect of the halogen bond to nitrogen, chloride, bromide, and iodide in terms of the chemical shift of the carbon covalently bonded to iodine, and the acetylene carbon. The hydrogen bonds in these frameworks are characterized by ^{1}H SSNMR, enabling the identification of trends in terms of the hydrogen bonding to chloride, bromide, and iodide. The observation of the halides using ^{35}Cl and $^{79/81}$Br NMR is supported by natural localized molecular orbital (NLMO) DFT calculations, an extension of the natural bond orbital analysis.[52] This approach uses molecular orbitals familiar to chemists to explain the origins of the observed NMR parameters. The results are expressed as a sum of Lewis contributions, which parallel the Lewis dot structure, and non-Lewis contributions.[53]

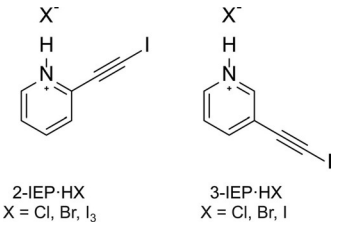

Figure 1. Compounds under investigation: 2-iodoethynylpyridine (2-IEP) and its HCl salt (2-IEP·HCl), HBr salt (2-IEP·HBr), HI_3 salt (2-IEP·HI_3); 3- IEP·HI)·iodoethynylpyridine (3-IEP) and its HCl salt (3-IEP·HCl), HBr salt (3-IEP·HBr), and HI salt (3-IEP·HI).

Results and Discussion

X-ray crystallography

Depictions of the X-ray crystal structures of the compounds under investigation are presented in Figure 2, and selected experimental crystallographic parameters are shown in Table S3. The triangular motif of the 2-IEP structure has been recently reported.[54,55] Each compound features a halogen bond, and in the cases of the halide salts, both halogen bonding and hydrogen bonding arise. A summary of the geometrical features for each compound, including the distances and angles of the halogen and hydrogen bonds, is given in Table 1.

Compounds 2-IEP·HCl and 2-IEP·HBr are isostructural and isomorphous, with each respective halide ion acting as both the halogen bond acceptor and hydrogen bond acceptor, resulting in charged dimers (Figure 2). The C–I···Cl^- halogen bond ($R_{XB} = 0.81$) is characterized by a slightly smaller reduced distance parameter than the C–I···Br^- halogen bond ($R_{XB} = 0.83$). This trend is also followed for the hydrogen bond lengths, with the analogous reduced distance parameters of the hydrogen bond (R_{HB}) being 0.75 for 2-IEP·HCl and 0.77 for 2-IEP·HBr. The halogen bond angle ($\theta_{C-I\cdots X^-}$) is very slightly more linear for 2-IEP·HCl versus 2-IEP·HBr, that is, 176.60(8)° compared to 175.75(10)°. The same holds for the hydrogen bond, with an angle ($\theta_{N-H^+\cdots X^-}$) of 159(2)° for 2-IEP·HCl and 155(3)° for 2-IEP·HBr. This counterintuitive decrease in angle with the size of the halide ion may be rationalized by considering the larger

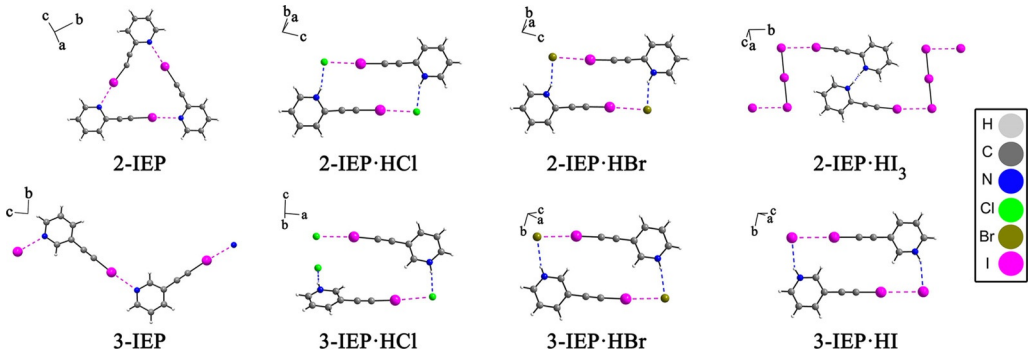

Figure 2. Depictions of the halogen bonded X-ray crystal structures of 2-iodoethynylpyridine (2-IEP), 3-iodoethynylpyridine (3-IEP), and their associated halide salts (HCl, HBr, HI, HI_3). The dashed magenta line denotes the halogen bond, whereas the dashed blue lines denote the hydrogen bonds. The geometrical details of these halogen bonds and hydrogen bonds are listed in Table 1.

Table 1. Summary of the halogen bond and hydrogen bond geometries of 2-IEP, 3-IEP, and their hydrohalide salts. The X represents the acceptor moiety: N, Cl^-, Br^-, or I^-. Errors are given in parentheses.

Compound	$d_{I\cdots X}$ [Å]	$d_{H\cdots X}$ [Å]	R_{XB}[b]	R_{HB}[b]	$\theta_{C-I\cdots X}$ [°]	$\theta_{N-H\cdots X^-}$ [°]	$\theta_{I\cdots X^-\cdots H}$ [°][c]
2-IEP	2.83(3)[a]		0.80		173.1(16)		
	2.84(2)[a]		0.80		177(2)		
	2.90(3)[a]		0.82		176.0(14)		
2-IEP·HCl	3.0217(8)	2.20(2)	0.81	0.75	176.60(8)	159(2)	94.1
2-IEP·HBr	3.1646(4)	2.36(3)	0.83	0.77	175.75(10)	155(3)	90.5
2-IEP·HI_3	3.448(4)		0.87		173.3(9)		
3-IEP	2.794(10)		0.79		176.0(3)		
3-IEP·HCl	3.1367(5)	2.16(2)	0.84	0.73	175.49(5)	171(2)	95.7
3-IEP·HBr	3.3001(4)	2.47(4)	0.86	0.81	169.31(9)	157(4)	87.7
3-IEP·HI	3.4713(7)	2.74(5)	0.88	0.86	170.3(2)	144(5)	89.3

[a] Three crystallographically distinct halogen bonds appear in the crystal structure of the 2-IEP trimer. [b] The normalized distance parameters of the halogen and hydrogen bonds. [c] The angle between the hydrogen and halogen bonds.

radius of the bromide ion, which elongates both the halogen bond and hydrogen bond, and strains the dimers.

In both 2-IEP·HCl and 2-IEP·HBr, the mixed halogen-bonded and hydrogen-bonded charged dimers are further assembled into supramolecular ribbons which develop along the (1,1,0) direction as shown in Figure 3. This arrangement is promoted by the hydrogen bonding interaction occurring between the belt of negative potential (labelled δ− in Figure 3) on the iodine atom and the aromatic hydrogen on the adjacent pyridinium ring (see Figure 3 for 2-IEP·HBr). It is known that when iodine is bound to a sp-hybridized carbon atom, iodine shows a remarkable anisotropic distribution of its electron density, developing an electron deficient area (σ-hole) along the elongation of the C–I bond and a belt of negative potential orthogonal to this bond. Additionally, the formation of the pyridinium moiety increases the Lewis acid character of the aromatic hydrogen atoms, making them good electron density acceptor sites (I1···H3 distance 3.11 Å in 2-IEP·HCl and 3.13 Å in 2-IEP·HBr). As a result, the C–I···X^- halogen bond synthon experiences a hydrogen bond coordinating the belt of negative potential surrounding the iodine halogen bond donor, and a hydrogen bond coordinating the Cl^-/Br^- acceptor. The resulting interactions create a ribbon-like motif as seen in Figure 3. As halide anions are spherical entities and are known to participate in many non-covalent interactions simultaneously, the charged ribbons interact via hydrogen bonding between the halide anions (Cl^- or Br^-) and the hydrogen atom, in the *ortho*-position relative to the N–H^+ moiety. These contacts result in the ribbons forming two-dimensional wave-like systems (Figure S8).

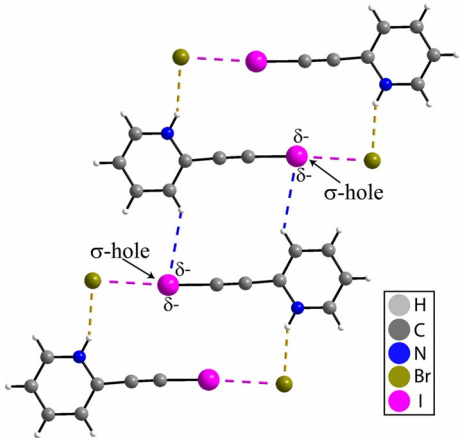

Figure 3. A supramolecular ribbon architecture is supported by C–I···Br^- halogen bonding (dashed magenta lines), N–H···Br^- hydrogen bonding (dashed brown lines) and C–H···I hydrogen bonding (dashed blue lines) interactions in 2-IEP·HBr. The σ-hole and the negative ESP on I are labelled.

2-IEP·HI was not obtained when repeating the synthesis with HI gas; instead, 2-IEP·HI_3 was obtained, perhaps due to the decomposition of HI gas into I_2. The structure of 2-IEP·HI_3 consists of an open framework, as shown in Figure 2, featuring a N–H^+···N hydrogen bond [$d_{N–H···N}$ = 1.805 Å, $\theta_{N–H···N}$ = 175.29°], and a halogen bond between the iodoacetylene group and the I_3^- anion [$d_{I···I}$ = 3.448(4) Å, $\theta_{C–I···I}$ = 173.3(9)°]. Due to a 0.5:0.5 partial occupancy of the hydrogen, we observe a superposition of N–H^+···N and N···$^+$H–N hydrogen bonds in the structural model. Overall, the structure shares a strong resemblance to the Greek keys motif as a result of the halogen bond to the first and third iodines of the I_3^- anion.

In contrast to the discrete triangular motif of 2-IEP, the crystal structure of 3-IEP displays an open zig-zag pattern with individual molecules linked together by C–I···N halogen bonds. The halogen bond distances are slightly shorter than those observed in 2-IEP ($d_{I···N}$ = 2.794(10) Å; $\theta_{C–I···N}$ = 176.0(3)°). The zig-zag networks interact via weak C–H···H–C contacts ($d_{H···H}$ = 2.31 Å), resulting in two-dimensional sheets. These sheets are stacked, forming the crystal of 3-IEP.

The structure of 3-IEP·HCl displays an open chain joined by C–I···Cl^- halogen bonds and N–H···Cl^- hydrogen bonds. The structure of 3-IEP·HCl is distinct from the 3-IEP·HBr and 3-IEP·HI structures, which consist of discrete charged dimers instead of an open framework. These charged dimers bear some resemblance to previously reported structures based on 3-bromopyridine.[56–59] Further, the ribbon motif reported for the 2-IEP·HCl and 2-IEP·HBr structures is also present in the 3-IEP·HBr and 3-IEP·HI structures. In these cases, the halides in the charged dimers are coordinated by the atoms in the *ortho*- and *meta*-positions relative to the N–H^+ moiety.

Throughout the 3-IEP·HX series presented here, the halogen bond distances and R_{XB} values increase as follows: 3-IEP·HCl (R_{XB} = 0.84), 3-IEP·HBr (R_{XB} = 0.86), 3-IEP·HI (R_{XB} = 0.88). The halogen bond angles ($\theta_{C–I···X^-}$) are most linear for 3-IEP·HCl, at 175.49(5)°, compared to 3-IEP·HBr at 169.31(9)°, and 3-IEP·HI at 170.3(2)°. Contrarily to the halogen bond, the hydrogen bond R_{HB} values differ considerably across the three structures, with values of 0.73, 0.81, and 0.86 for 3-IEP·HCl, 3-IEP·HBr, and 3-IEP·HI, respectively. The N–H^+···X^- hydrogen bond angles also vary, with the most linear hydrogen bond being that of 3-IEP·HCl at 171(2)°, followed by 3-IEP·HBr at 157(4)°, and 3-IEP·HI at 144(5)°.

The C–I···N halogen bonds of the neutral species consistently have the smallest R_{XB} values when compared to the charged samples, ranging between 0.79 and 0.82. Additionally, the C–I···N halogen bonds are the most linear, with $\theta_{C–I···N}$ angles between 173.1(16)° and 177(2)°. With regards to the halogen bonds involving the halides, the C–I···Cl^- halogen bond consistently had the smallest R_{XB} values when compared to the C–I···Br^- and C–I···I^- halogen bond, with the measured R_{XB} values increasing with the size of the halogen. These R_{XB} values are comparable to those for other structures featuring the C≡C–I···X^- motif.[26,50] For the N–H^+···X^- hydrogen bonds, the value of R_{HB} increased with the size of the halides, with 3-IEP·HCl having the smallest R_{HB} at 0.73, and 3-IEP·HI having the largest R_{HB} at 0.86. Notably, whereas the halogen bond angles range from 169.31(9)° to 177(2)°, a difference of 8(2)°, the hydrogen bond angle varies significantly, from 144(5)° to 171(2)°, a difference of 27(5)° across the series.

The charged dimers of 2-IEP and 3-IEP share many structural features, including the C–I···X^-···H–N^+ geometry surrounding the halide. Despite 3-IEP·HCl consisting of an open framework, the hydrogen and halogen bonds to the chloride anion share several geometrical features with the 2-IEP·HCl discrete dimer, such as $\theta_{I···X^-···H}$ values of 95.7° and 94.1°, respectively. Consequently, the halogen bonds and hydrogen bonds involving chloride, bromide, and iodide ions can be compared in terms of NMR observables. Although the neutral species (2-IEP, 3-IEP) do not share the same structural motifs as their halide salts, the C–I···N halogen bonds can be compared to the C–I···X^- halogen bonds in terms of ^{13}C chemical shifts of the carbon covalently bonded to iodine (C–I), and the acetylene carbon (C≡C–I).

^{1}H solid-state NMR spectroscopy

With the availability of high magic-angle spinning speeds, ^{1}H solid-state NMR has become a routine tool to characterize hydrogen bonded systems.[60,61] The ^{1}H MAS NMR spectra of 2-IEP·HI_3, 2-IEP·HBr, 2-IEP·HCl, 3-IEP·HI, 3-IEP·HBr, and 3-IEP·HCl are presented in Figure 4. The ^{1}H chemical shifts of the NH

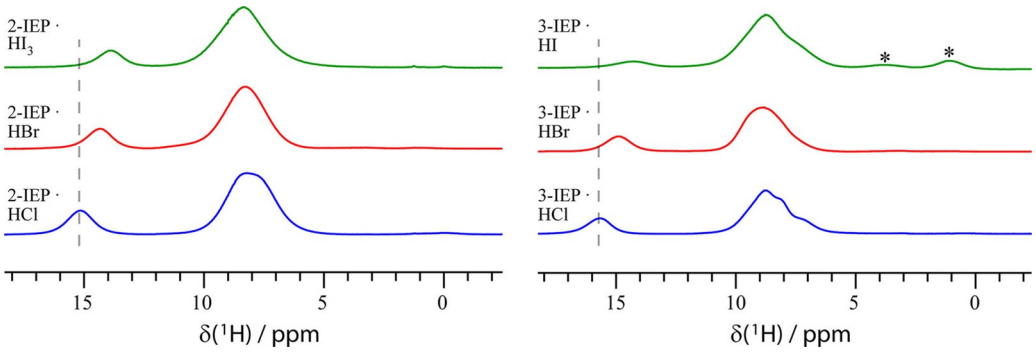

Figure 4. ^{1}H solid-state NMR spectra acquired at 21.1 T of the halide salts of 2-IEP and 3-IEP. The spectra of the HCl and HBr salts were acquired with a spinning frequency of 31.25 kHz, whereas those of the HI and HI_3 salts were acquired with a spinning frequency of 20 kHz. The dashed line serves as a guide to show the chemical shift of the hydrogen-bonded proton changes. The asterisks denote an impurity.

Table 2. Experimental and calculated ^{1}H chemical shifts of the N–H proton participating in the hydrogen bond in the halide salts of 2-IEP and 3-IEP.

Compound	Exptl $\delta(^1H)$ *N–H* [ppm]	Calcd $\delta(^1H)$ *N–H* [ppm]
2-IEP·HCl	15.14 ± 0.23	13.99
2-IEP·HBr	14.35 ± 0.24	12.79
2-IEP·HI_3	13.88 ± 0.21	13.39
3-IEP·HCl	15.68 ± 0.22	15.99
3-IEP·HBr	14.89 ± 0.18	14.80
3-IEP·HI	14.28 ± 0.30	13.70

protons are reported in Table 2. The following discussion focuses on the N–H proton, as it is directly participating in the N–H···X^- hydrogen bond. Within each series, a notable decrease in the ^{1}H chemical shift is observed as the size of the halide increases. For instance, the ^{1}H chemical shift for the 3-IEP·HX series decreases by 1.4 ± 0.4 ppm when comparing the chloride salt to the iodide salt. When comparing the 3-IEP·HCl salt to the HBr salt, a decrease of 0.8 ± 0.3 ppm is observed, approximately half of the shift observed for the iodide salt. This trend is also observed in the 2-IEP series, with a decrease of 0.8 ± 0.3 ppm when comparing the HCl salt to the HBr salt. It is to be noted that in the case of 2-IEP·HI_3, the ^{1}H chemical shift is also lower than for 2-IEP·HCl, despite the presence of a N–H···N hydrogen bond instead of a N–H···X^- hydrogen bond. The decreases in the ^{1}H chemical shifts upon the introduction of larger halides can be, in part, attributed to the heavy atom-light atom (HALA) effect, arising from increasing relativistic effects with the size of the halogen.[62–64]

To further look into the origin of this deshielding effect upon the introduction of larger halides, DFT calculations using ZORA corrections were performed on a model of each compound built from experimental Cartesian coordinates, both before and after geometry optimization. The complete results can be found in Table S4 (unoptimized geometry) and Table S5 (geometry optimized), listing the molecular orbital contributions to the isotropic shielding constant (σ_{iso}) of the $^+$N–H···X^- hydrogen bonded proton for each compound. The results were tabulated according to their molecular orbital contributions to σ_{iso}: core orbital contributions, halide ion lone pair contributions, N–H bonding orbital contributions, and bonding orbital contributions arising from all other atoms. The calculated $\sigma_{iso}(^1H)$ shielding values from the optimized geometries have been converted into chemical shifts ($\delta_{iso}(^1H)$) using Equation (4), in which σ_{ref} is 26.293 ppm,[65] and summarized alongside the experimental ^{1}H chemical shifts in Table 2.

$$\delta_{iso} = \frac{\sigma_{ref} - \sigma_{iso}}{1 - \sigma_{ref}} \quad (4)$$

Consequently, a higher shielding value (σ_{iso}) results in a lower chemical shift (δ_{iso}).

The calculated proton chemical shifts obtained from geometry-optimized structures are in good agreement with the experimental results, and better than the calculations performed on structures which were not geometry-optimized. In part, this is due to the correction of the N–H bond length, as proton positions obtained from X-ray crystallography have an associated uncertainty.[66,67] Moreover, the DFT results accurately reproduce the experimental trend that a decrease in the value of the proton chemical shift is seen as the size of the halide ion is increased. However, the calculated results for 2-IEP·HI_3 do not follow the above-mentioned trend, which we speculate is due to the presence of a $^+$N–H···N hydrogen bond in this structure instead of the $^+$N–H···X^- hydrogen bonds observed in the crystal structures of the other salts in the 2-IEP and 3-IEP series.

NLMO analysis of the proton magnetic shielding constants shows that the dominant orbital contribution to the $^+$N–^{1}H···X^- chemical shift changes is different in the 2-IEP series compared to the 3-IEP series. In the 2-IEP series, the halide ion lone pair contributions to σ_{iso} are largest in magnitude in the case of the chloride compound and smallest in the case of the iodide compound, corresponding to a decrease of the proton chemical shift as the size of the halide ion is increased. However, in the case of the 3-IEP series, the sum of bonding orbital contributions to σ_{iso} were found to be the most important for reproducing the experimentally observed trend, that is, to a decrease of the proton chemical shift as the size of the halide ion is increased. The more than 40 additional NLMO contributions to the ^{1}H magnetic shielding constants are not discussed further here due to their small magnitudes and lack of clear correlations to the total σ_{iso} values.

^{13}C Solid-state NMR spectroscopy

^{13}C SSNMR spectroscopy has been shown to be a versatile tool in characterizing both the halogen bond acceptor and the halogen bond donor, with the ^{13}C–I chemical shift being diagnostic for the occurrence of the halogen bond.[32,68] However, it is challenging to differentiate the effect of altering the identity of the halogen bond acceptor on the donor ^{13}C chemical shift, due to the fact that structural changes, such as the proximity of adjacent atoms and changes to the unit cell, can also have an effect on the ^{13}C chemical shifts. Therefore, isomorphous compounds sharing similar unit cell parameters, such as the compounds presented here, provide a means to attribute chemical shift changes to the identity of the bond acceptor, that is, Cl^-, Br^-, or I^-. Moreover, despite the fact that the neutral fragments are not isostructural and do not share similar unit cell parameters, the ^{13}C–I chemical shift can be used to compare the halogen bond involving nitrogen to the halogen bond involving a halide.

Presented in Figure 5 are the ^{13}C SSNMR spectra of 2-IEP, 3-IEP, and their halide salts, with a magnified view of the carbon resonance corresponding to the C–I carbon in the insets. As a result of residual dipolar coupling between ^{13}C and ^{127}I, the ^{13}C resonance for a C–I functional group is generally broadened and difficult to observe.[31,69,70] This is further aggravated by the quadrupolar nature of ^{127}I (spin $I = 5/2$) and the substantial C_Q values (> 1800 MHz) associated with covalently bonded iodine.[71] Although the resonances assigned to the C–I carbons on Figure 5 are broad and have a low signal intensity relative to the other resonances, they were clearly observed, and the

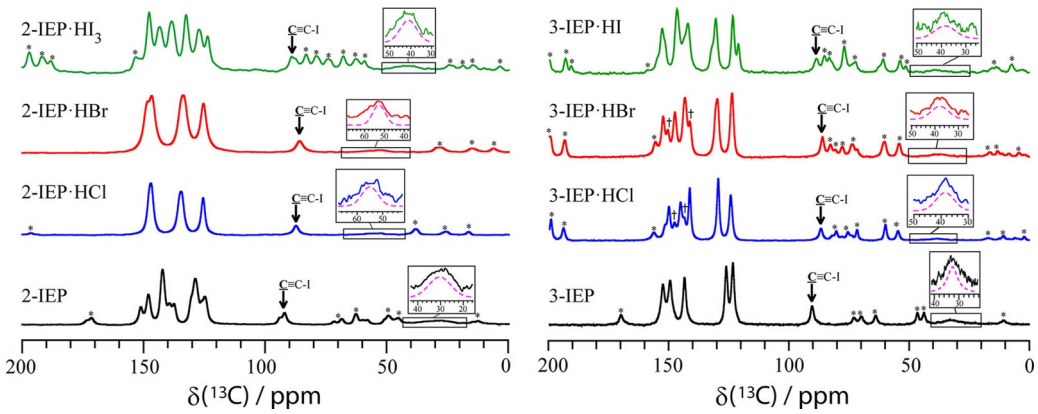

Figure 5. ^{13}C CP/MAS solid-state NMR spectra of 2-IEP, 3-IEP, and their hydrohalide salts. Variable spinning frequencies were used to prevent the overlap of spinning sidebands with the isotropic peaks. The magnified view of the C—I carbon resonance is shown in the inset. The asterisks denote spinning sidebands, while the daggers (†) denote the presence of a second phase.

^{13}C chemical shifts were determined using spectral simulations with WSolids software.[72] Due to the overlap of spinning sidebands with the isotropic chemical shifts, variable spinning speeds were used to separate the spinning sidebands from the isotropic peaks. The experimental and DFT calculated ^{13}C chemical shifts of the acetylene carbon (C≡C—I) and the carbon covalently bonded to iodine (C—I) of each compound are summarized in Table 3. In the aromatic region (≈140 to 160 ppm) of the spectra of 3-IEP·HCl and 3-IEP·HBr, the presence of resonances, denoted by †, are attributed to be the presence of a second phase in the sample. This second phase is also seen in the corresponding ^{35}Cl and $^{79/81}Br$ SSNMR spectra (vide infra).

A significant ^{13}C—I chemical shift increase was observed between 2-IEP and each of the halide salts. Most notably, ^{13}C chemical shift increases for the C—I carbon of 27.1 ± 3.2 ppm when comparing 2-IEP to 2-IEP·HCl, 24.7 ± 2.6 ppm comparing 2-IEP to 2-IEP·HBr, and 13.4 ± 3.2 ppm comparing 2-IEP and 2-IEP·HI_3, were observed. For 3-IEP, a modest ^{13}C chemical shift increase was observed for the C—I carbon when comparing the neutral compound to that of the charged frameworks, with increases of 5.9 ± 1.4 ppm, 5.4 ± 1.9 ppm, and 5.9 ± 2.4 ppm seen for 3-IEP·HCl, 3-IEP·HBr, and 3-IEP·HI, respectively. In both the 2-IEP and 3-IEP series, the C—I···N halogen bond yielded the lowest chemical shift, and the C—I···Cl^- halogen bond yielded the highest chemical shift. Thus, especially in the case of the 2-IEP series, the counter ion has an important influence on the C—I chemical shift, with a 13.7 ± 3.3 ppm difference between 2-IEP·HCl and 2-IEP·HI_3.

Table 3. Experimental and DFT calculated ^{13}C chemical shifts of the acetylene carbon (**C**≡C—I) and the carbon covalently bonded to iodine (**C**—I) for 2-IEP, 3-IEP, and their hydrohalide salts.

	Exptl $\delta(^{13}C)$ **C**≡C—I [ppm]	Calcd $\delta(^{13}C)$ **C**≡C—I [ppm][a]	Exptl $\delta(^{13}C)$ **C**—I [ppm]	Calcd $\delta(^{13}C)$ **C**—I [ppm]
2-IEP	91.9 ± 0.2 93.6 ± 0.4	96.4	27.9 ± 2.2	39.9
2-IEP·HCl	87.2 ± 0.1	89.5	55.0 ± 2.3	93.4
2-IEP·HBr	85.8 ± 0.2	87.7	52.6 ± 1.3	91.2
2-IEP·HI_3	89.0 ± 0.2	74.6	41.3 ± 2.3	68.7
3-IEP	90.5 ± 0.2	93.4	32.6 ± 1.1	40.2
3-IEP·HCl	86.8 ± 0.2	89.8	38.5 ± 0.9	71.5
3-IEP·HBr	87.0 ± 0.2	87.9	38.0 ± 1.5	73.2
3-IEP·HI	88.9 ± 0.4	84.3	38.5 ± 2.1	65.7

Although the acetylene carbon (**C**≡C—I) does not directly participate in the halogen bond, its NMR response can provide valuable insights on the effect of the halogen bond on nearby substituents. Instead of an increase, as was noted above for the C—I ^{13}C chemical shift, a notable decrease in the ^{13}C chemical shift was observed for the acetylene carbon between the neutral fragments and the charged fragments. In this case, the neutral compounds exhibiting C—I···N halogen bonds have the highest ^{13}C chemical shifts at 91.9 ± 0.2 ppm and 90.5 ± 0.2 ppm for 2-IEP and 3-IEP, respectively. Upon introduction of the C—I···Cl^- halogen bond, the chemical shifts decreased to 87.2 ± 0.1 and 86.8 ± 0.2 ppm for 2-IEP and 3-IEP, respectively. In general, the chemical shift of the acetylene carbon in the charged dimers increases with the size of the halogen. The only exception is 2-IEP·HBr, which has the lowest chemical shift of 85.8 ± 0.2 ppm. For instance, between 3-IEP·HCl and 3-IEP·HI, a 2.1 ± 0.4 ppm difference in the ^{13}C chemical shift is observed, with the HCl salt having the lowest chemical shift. This trend follows for the halogen bond to Cl^- and I_3^-, as an increase of 1.8 ± 0.2 ppm is observed between 2-IEP·HCl and 2-IEP·HI_3.

The experimental ^{13}C chemical shifts are in good agreement with the ZORA DFT calculated chemical shifts for the acetylene carbons (**C**≡C—I), and in moderate agreement for the carbons covalently bonded to iodine (**C**—I). Given the broad chemical shift range associated with the ^{13}C isotope (≈250 ppm), the calculated acetylene chemical shifts are generally within 2% of the experimental values, while those for the C—I carbon are within 15% of the experimental values. The poorer agreement for the latter functional group has been previously discussed in the literature and can be attributed to iodine's relativistic effects,[73] in spite of attempting to correct for this using ZORA.[68,74] Despite this lower accuracy for the C—I carbon, the calculated ^{13}C chemical shifts do reflect the changes observed

experimentally, such as the significant increase in the ^{13}C chemical shift of the C–I carbon on going from the neutral C–I···N structures (2-IEP, 3-IEP) to the charged C–I···Cl^- structures (2-IEP·HCl, 3-IEP·HCl).

The NLMO analysis of the ^{13}C isotropic shielding constants suggests that the origins of the chemical shift changes may be similar in the case of the 2-IEP compounds and the 3-IEP compounds (see Tables S6 to S9 in the Supporting Information), in contrast to the case of the ^{1}H chemical shifts. Firstly, for the C–I carbon, there are four principal contributions to the ^{13}C isotropic shielding constant (σ_{iso}): carbon core orbitals, the bonding orbitals involving the acetylene carbon (the C≡C bond), the bonding orbital involving iodine, and the antibonding C–I orbital. Recall that an increased value of σ_{iso} results in a lower chemical shift. Following from the results in Table S7, in both series, the C–I bonding orbital contribution, which is negative in sign, increases in magnitude on going from the C–I···N motif to the C–I···X^- motif, causing σ_{iso} to decrease, and, consequently, δ_{iso} to increase. For instance, the contribution to σ_{iso} from the C–I bonding orbital is −54.6 ppm in 2-IEP, and increases in magnitude to −75.2 ppm in 2-IEP·HCl. Additionally, the contributions from the bonding orbitals involving the acetylene carbon (C≡C) also increase in magnitude upon the formation of the C–I···X^- motif, which further increases with the size of the halide ($I^- > Br^- > Cl^-$). For instance, the acetylene contribution to σ_{iso} is −20.2 ppm in 2-IEP, −43.4 ppm in 2-IEP·HCl, and −47.2 ppm in 2-IEP·HBr. Moreover, the C–I anti-bonding orbital contribution to σ_{iso} is generally larger in the C–I···N motif than the C–I···X^- motif, further leading to a lower δ_{iso} for the former. Following with the previous example, the C–I anti-bonding orbital contribution to σ_{iso} decreases from 20.5 ppm in 2-IEP to 16.9 ppm in 2-IEP·HCl. In total, the C–I and C≡C orbital contributions lead to a decrease in the σ_{iso} value, from 144.2 ppm in 2-IEP to 90.7 ppm in 2-IEP·HCl, and consequently the δ_{iso} value increases from 39.9 ppm in the C–I···N motif to 93.4 ppm in the C–I···Cl^- motif. These changes are generally greatest when Cl^- is the halogen bond acceptor, leading to the highest observed ^{13}C–I chemical shift in this motif.

This effect is further manifested in the case of the acetylene carbons (C≡C–I), where the contributions of the C–I bonding orbitals cause σ_{iso} to decrease upon the formation of the C–I···X^- motif, being most important in the case of the Cl^- anion and least important for the I^- anion. Following with the results from Table S9, the bonding orbital contributions involving the C–I carbon, which are negative in sign, increases in magnitude on going from the C–I···N motif to the C–I···X^- motif. For instance, this contribution is −37.3 ppm in 2-IEP and increases to −41.9 ppm in 2-IEP·HCl. Consequently, the calculated ^{13}C≡C–I chemical shifts decrease from 96.4 ppm in 2-IEP, to 89.5 ppm in 2-IEP·HCl. It is to be noted that the contributions to σ_{iso} of the acetylene carbon from the bonding orbitals involving the pyridine ring varies between each compound, being lowest for 3-IEP·HCl and highest for 3-IEP·HI.

^{35}Cl and $^{79/81}Br$ solid-state NMR spectroscopy

In order to further characterize the halogen bonding environments in the charged dimers, ^{35}Cl and $^{79/81}Br$ solid-state NMR spectroscopy was performed on the HCl salts and HBr salts, respectively. Due to difficulties in isolating large quantities of pure 2-IEP·HI_3 and 3-IEP·HI (and their thermal instabilities), along with the expected breadths of the NMR spectra, ^{127}I solid-state NMR was not attempted. The experimental ^{35}Cl and ^{81}Br spectra at 21.1 T were fit with QUEST[86] and are shown in Figure 6. The ^{35}Cl MAS spectra and the ^{79}Br spectra are shown

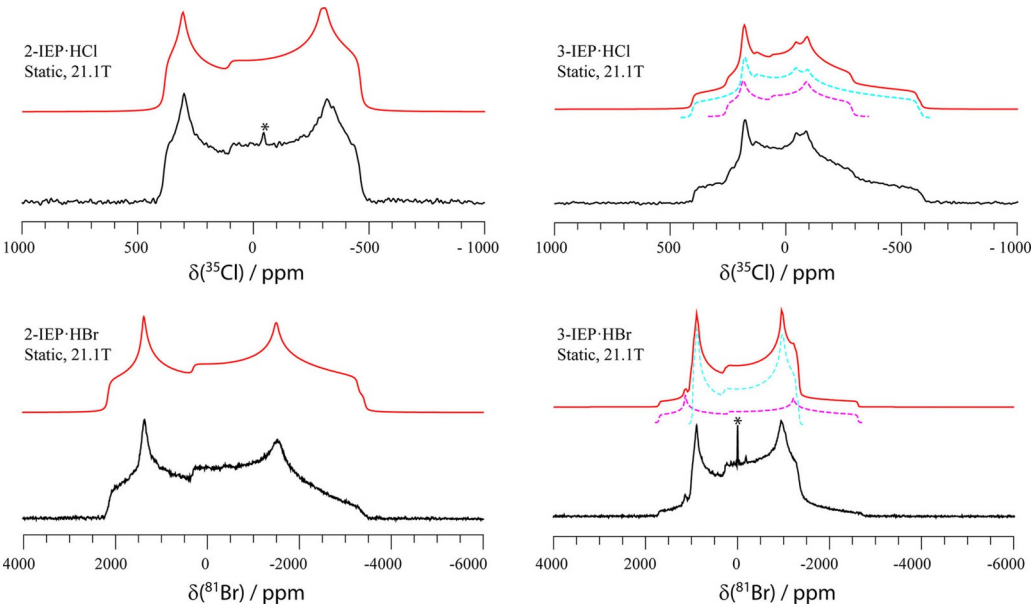

Figure 6. ^{35}Cl and ^{81}Br solid-state NMR at 21.1 T of 2-IEP·HCl, 3-IEP·HCl, and 2-IEP·HBr, 3-IEP·HBr, respectively. The experimental spectra are shown in black, and the red traces denote the simulated spectra. Deconvoluted simulated spectra are shown in dashed magenta and dashed cyan for 3-IEP·HCl and 3-IEP·HBr. Asterisks denote minor impurities. Difference spectra may be found in the Supporting Information.

in Figures S17 and S18. Additionally, DFT calculations (see the Experimental Section for details) were performed on cluster models of each compound to support the empirical results with a theoretical model, providing a breakdown of the molecular orbital contributions to the EFG at each halide. Although ^{127}I SSNMR spectroscopy was not feasible in these cases, NLMO calculations were performed in order to compare the EFG at each halide ion. Although the 2-IEP·HI structure was not obtained experimentally, a theoretical model of the 2-IEP·HI dimer was built based on the coordinates for 2-IEP·HBr in order to have a complete NLMO investigation of all the stable quadrupolar halides. In addition, a dimeric model of the 3-IEP·HCl was built based on the coordinates for 3-IEP·HBr to maintain consistency between all the calculations. It is to be noted that other contacts to the halides, such as the H···Cl contact discussed in the X-ray section, are not taken into account in our calculations in effort to isolate the effect the hydrogen and halogen bonding effects on the EFG. This lack of periodicity in the calculations is manifested in a lower agreement between experimental and calculated results, but did not impede the analysis.

Reasonable ^{35}Cl signal intensity was obtained for both samples, both in MAS and static experiments. The resulting ^{35}Cl chemical shift and quadrupolar coupling parameters of 2-IEP·HCl and 3-IEP·HCl, summarized in Table 4, reveal the similarities between both chloride ion environments. There are small differences of 14 ± 8 ppm and of 0.47 ± 0.09 MHz in the ^{35}Cl chemical shift and C_Q values, respectively. Such small differences are reasonable, considering the two salts share the same C–I···Cl$^-$···H–N$^+$ moiety. However, real differences in the halogen bonding and hydrogen bonding geometry between 2-IEP·HCl and 3-IEP·HCl are manifested in the η values and the chemical shift anisotropy parameters (Ω, κ), along with the Euler angles (α, β, γ). In the case of 3-IEP·HCl, a minor impurity was present which is attributed to the formation of a different polymorph, given the similarity of the NMR parameters [C_Q = 4.85 MHz, $\eta = 0.40$, $\delta_{iso} = 70$ ppm, $\Omega = 35$ ppm, $\kappa = 0$, $\alpha = 30^\circ$, $\beta = 10^\circ$, $\gamma = 30^\circ$]. According to the signal intensity, the concentration of this second polymorph is of approximately 10%, and did not impede analysis. The trace impurity in 2-IEP·HCl, denoted by an asterisk, is NaCl(s), given its chemical shift and narrow line width.

Much like the ^{35}Cl NMR spectra, both the static ^{81}Br (Figure 5) and ^{79}Br (Figure S18) solid-state NMR spectra of 2-IEP·HBr and 3-IEP·HBr had reasonable signal intensities considering their large spectral widths. As bromine has two NMR active isotopes with unique quadrupole moments ($Q(^{81}\text{Br}) = 262(3)$ mb, $Q(^{79}\text{Br}) = 313(3)$ mb),[75] two different values of C_Q are expected [see Eq. (2)]. However, the EFG at both nuclides should be the same, with the resulting C_Q arising solely due to the difference in quadrupole moments. Therefore, the C_Q obtained from ^{79}Br NMR should be in agreement with the ^{81}Br NMR results after scaling by a factor of ≈ 1.19 [$Q(^{79}\text{Br})/Q(^{81}\text{Br})$], allowing us to verify the goodness of the spectral fitting. The trace impurity in 3-IEP·HB is NaBr(s), due to its chemical shift.

Comparing the NMR parameters between the bromide salts, 2-IEP·HBr has higher C_Q and δ_{iso} values versus 3-IEP·HBr. This bears resemblance to the comparison between 2-IEP·HCl and 3-IEP·HCl, in which case the former also had a higher value of C_Q and δ_{iso}. In contrast, the η values are not comparable between the chloride and bromide samples, perhaps due to the different contributions to $|V_{22}|$ and $|V_{11}|$. In addition, much like the 3-IEP·HCl sample, a minor impurity was measured in 3-IEP·HBr, which is also attributed to the occurrence of a different polymorph due to the similarities of the NMR parameters [$C_Q[^{81}\text{Br}] = 38.9$ MHz, $C_Q[^{79}\text{Br}] = 47.0$ MHz, $\eta = 0.34$, $\delta_{iso} = 200$ ppm]. According to the signal intensity, the concentration of this second polymorph is approximately 15%, and did not impede analysis.

Although the C_Q values for each of the halide ions are not immediately comparable, the $|V_{33}|$ eigenvalues can be extracted using Equation (2). As a result of the different electronic configurations of the halides, most importantly the inner-shell electrons, the Sternheimer antishielding factor may also be considered using Equation (4), as it has been shown to have a considerable impact on the observed EFG at a nucleus.[76,77]

$$eq_{obs} = (1 - \gamma_\infty) eq_{lattice} \quad (5)$$

In Equation (5), the observed EFG (eq_{obs}) is related to the lattice EFG ($eq_{lattice}$) by an antishielding factor (1-γ_∞). The antishielding factor has a value of 43.0, 81.0, and 163.0 for $^{35/37}$Cl, $^{79/81}$Br, and ^{127}I, respectively.[78] The comparison of the EFG across the halides will allow for the electronic charge distributions at the halide participating in a hydrogen and halogen bond in the C–I···X$^-$···H–N$^+$ motif to be compared. An NLMO analysis was performed in order to quantify the contributions

Table 4. Experimental ^{35}Cl and ^{79,81}Br solid-state NMR parameters for the hydrochloride salts and hydrobromide salts of 2-IEP and 3-IEP.

	$\lvert C_Q \rvert$ [MHz]	$\lvert V_{33} \rvert$ [a.u.]	η	δ_{iso} [ppm][a]	Ω [ppm]	κ	α [°]	β [°]	γ [°]
2-IEP·HCl	6.65 ± 0.08	0.347 ± 0.004	0.15 ± 0.03	86 ± 6	40 ± 10	-0.2 ± 0.2	90 ± 40	90 ± 30	30 ± 20
3-IEP·HCl	6.18 ± 0.05	0.322 ± 0.003	0.61 ± 0.04	72 ± 5	70 ± 10	-0.6 ± 0.1	90 ± 10	80 ± 20	25 ± 10
2-IEP·HBr	(^{79}Br) 52.4 ± 0.04 (^{81}Br) 43.5 ± 0.04	0.730 ± 0.002	0.34 ± 0.03	250 ± 15	200 ± 60	0.5 ± 0.5	90 ± 50	55 ± 30	130 ± 20
3-IEP·HBr	(^{79}Br) 37.5 ± 0.05 (^{81}Br) 31.2 ± 0.04	0.520 ± 0.002	0.14 ± 0.03	215 ± 20	200 ± 50	0 ± 0.5	25 ± 5	80 ± 5	10 ± 10

[a] ^{35}Cl chemical shifts are referenced to -41.11 ppm relative to NaCl(s), whereas ^{79}Br and ^{81}Br chemical shifts are referenced to 1.29 ppm and 1.57 ppm relative to NaBr(s), respectively.

to the $|V_{33}|$, $|V_{22}|$, and $|V_{11}|$ eigenvalues, summarized in Tables S11, S13, and S15, respectively. This analysis serves as a complement to previous computational studies,[79–81] and analysis on NLMO contributions to the EFG,[34] with a focus on the differences between halide halogen bond acceptors. In this motif, the most important contributions to the EFG at the halides are: the core orbital contributions, lone pair orbital contributions, iodine bonding orbital contributions, and bonding orbital contributions involving the hydrogen bond. In order to compare the EFG across each halide, a consistent dimeric model was used for each compound, including theoretical dimeric models of 2-IEP·HI and 3-IEP·HCl.

Illustrated in Figure 7, the computational results for each geometry optimized discrete dimer reveal that the $|V_{33}|$ eigenvector is oriented perpendicularly to the axis of the dimer, the $|V_{22}|$ eigenvector is oriented towards the halogen bond donor,

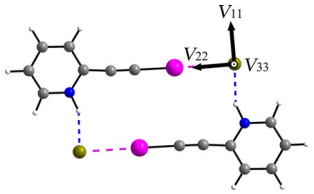

Figure 7. The bromine quadrupolar coupling tensor orientation of 2-IEP·HBr following a geometry optimization, showing $|V_{33}|$ oriented perpendicular to the plane of the dimer (towards the reader), $|V_{22}|$ aligned with the halogen bond, and $|V_{11}|$ oriented along the hydrogen bond.

and the $|V_{11}|$ eigenvector is aligned with the hydrogen bond. This orientation holds for each dimer, including the theoretical model of 2-IEP·HI. However, in the case of the dimeric model of 3-IEP·HCl, while $|V_{33}|$ remains oriented perpendicular to the dimer, the $|V_{22}|$ and $|V_{11}|$ eigenvectors deviate slightly from the halogen bond and hydrogen bond, respectively. As the eigenvectors have a consistent orientation towards the halogen bond or the hydrogen bond, a breakdown of the contributions to the EFG tensor for each halide offers insights into the molecular orbitals participating in these interactions. As for the calculations performed using experimental X-ray coordinates, $|V_{33}|$ is instead aligned with the halogen bond, $|V_{22}|$ is oriented perpendicular to the dimer, and $|V_{11}|$ remains aligned with the halogen bond. As the $|V_{33}|$ and $|V_{22}|$ eigenvectors have similar magnitudes, small changes in the local geometry, such as the correction of the N–H bond length, can contribute to the reorientation of the EFG tensor.

Following with the results using optimized geometries, the most important contribution to the $|V_{33}|$ eigenvector of the halide are the lone pair orbitals, followed by the core orbitals. The lone pair orbitals originating from the halogen bond donor did not have an important contribution (<6%), perhaps due to the eigenvector's orientation being perpendicular to the dimer. Furthermore, the calculations suggest that the halide's lone pair orbitals have the greatest relative contribution in $Br^- > I^- > Cl^-$. For instance, in the 3-IEP series, the relative contribution of the lone pair orbitals to $|V_{33}|$ for 3-IEP·HBr, 3-IEP·HCl, and 3-IEP·HI is of 92.4, 89.4, and 81.8%.

As for the $|V_{22}|$ eigenvector, which is oriented along the halogen bond, a significant negative contribution arises from the lone pair orbitals of the iodine from the halogen bond donor. Taking the 2-IEP series for example, the relative contribution from the halogen bond donor is most important in 2-IEP·HCl (12.5%), followed by 2-IEP·HBr (10.3%), and finally 2-IEP·HI (7.7%). These results suggest that in these compounds, the halogen bond has the highest relative contribution in the order of $Cl^- > Br^- > I^-$. This may support the reduction in the EFG tensor component oriented towards the halogen bond, with the relative contribution being largest for the chloride salts, and smallest in the iodide salts. Furthermore, while iodine's lone pair orbitals had a negative contribution to the $|V_{22}|$ eigenvector, they had a positive contribution to the $|V_{11}|$ and $|V_{33}|$ eigenvectors.

For the $|V_{11}|$ eigenvector, which is aligned with the hydrogen bond, the most important contributions are from the halide's lone pair orbital, followed by the core and bonding orbitals involving the nitrogen from the hydrogen bond. In these cases, however, the contributions from the hydrogen bond fluctuated considerably between samples. Clearly, however, the hydrogen bond had a negative contribution to $|V_{11}|$, with the magnitude generally increasing with the size of the halogen. For instance, for the 3-IEP series, the contribution for the HCl, HBr, and HI salts is 5.4, 16.0, and 29.5%, respectively. These results suggest a relative contribution from the hydrogen bond to the EFG component in the order of $I^- > Br^- > Cl^-$ in these compounds, in stark contrast of the trend observed for the halogen bond.

Shown in Figure 8 is a summary of the calculated and experimental $|V_{33}|$ eigenvalues for each halide in the 2-IEP and 3-IEP dimers. The overall EFG is largest in the iodide salts, followed by the bromide salts, and finally the chloride salts. Accounting for the Sternheimer antishielding factor for the HCl and HBr salts, shown in Figure S20, the relative $|V_{33}|$ for the 2-IEP series increases in the order of $Br^- > Cl^-$, both experimentally and computationally.

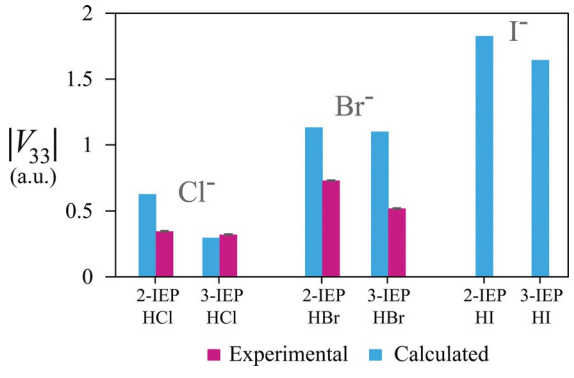

Figure 8. Experimental (magenta) and calculated (blue) $|V_{33}|$ of 2-IEP·HX and 3-IEP·HX (X = Cl^-, Br^-, I^-). The charged dimeric model was used in all calculations for consistency.

Conclusions

The crystal structures for a series of halide salts built from 2-iodoethynylpyridine (2-IEP) and 3-iodoethynylpyridine (3-IEP) are reported, featuring the cooperation of hydrogen and halogen bonds. In these compounds, the halogen bond maintains linearity, with an 8.85(9)° deviation in $\theta_{C-I\cdots X^-}$ across the series, whereas the hydrogen bond angle varies by 27(5)°. This is well in line with the higher directionality of halogen bond compared to the hydrogen bond. Each compound was investigated by multinuclear solid-state NMR: ^{1}H to investigate the nature of the hydrogen bond, ^{13}C to investigate the nature of the halogen bond, along with ^{35}Cl and $^{79/81}$Br to investigate the halogen bond acceptor. The ^{1}H SSNMR results show a shielding of the hydrogen bond donor as the size of the halogen increases, whereas the ^{13}C SSNMR shows a large chemical shift increase of the C–I carbon upon going from the C–I···N motif to the C–I···X$^-$ motifs. A direct investigation of the halide halogen bond acceptor by SSNMR, in addition to NLMO calculations, reveals an increase in the electric field gradients with the size of the halogen, summarized in Figure 8. Computational results from dimeric models suggest that, in this motif, the EFG eigenvector $|V_{22}|$ is oriented towards the halogen bond donor, whereas the smallest component of the EFG tensor, $|V_{11}|$, is oriented towards the hydrogen bond. In these compounds, the relative contribution to $|V_{22}|$ from the halogen bond increases in the order of $Cl^- > Br^- > I^-$, in contrast to the relative contributions to $|V_{11}|$ from the hydrogen bond, in the order of $I^- > Br^- > Cl^-$.

We speculate that the agreement between the experimental and computational data reported in this work could be further improved in the future by simultaneously invoking periodic boundary conditions along with higher-level relativistic effects while maintaining dispersion corrections.

Overall, this work demonstrates from crystal engineering and multinuclear solid-state magnetic resonance perspectives the relative influences and roles of halogen and hydrogen bonds. In the case of the former, the interplay of the two interactions resulted in a range of supramolecular architectures ranging from triangles to dimers to open chains and supramolecular wavy ribbons. From the solid-state NMR perspective, interaction tensor magnitudes and orientations have been demonstrated to be exquisitely sensitive to the two types of interactions and the role of different halogen bond donor moieties in determining the NMR response has been elucidated.

Experimental Section

2-Ethynylpyridine (98%), 3-ethynylpyridine (98%), phosphorus pentoxide (98%), anhydrous calcium chloride (96+%), aqueous HBr (42%), and aqueous HI (57%) were purchased from Sigma Aldrich and used without further purification. Aqueous HCl (38%) and all solvents were purchased from Fisher Scientific. 2-Iodoethynylpyridine[54] and 3-iodoethynylpyridine were synthesized using a literature procedure.[82] [3-iodoethynylpyridine: ^{1}H NMR ([D$_4$]MeOH, TMS, 300 MHz) 8.56, 8.47, 7.85, 7.40 ppm; ^{13}C NMR ([D$_4$]MeOH, TMS, 300 MHz) 153.2, 149.3, 141.2, 124.9, 122.7, 90.4, 17.6 ppm. HREI-MS: *m/z* elemental analysis calcd (%) for C_7H_4IN $[M]^+$: 228.938, found: 228.939]

The hydrohalide salts of 2-IEP and 3-IEP were produced by dissolving the appropriate compound in anhydrous ether and bubbling the hydrohalic acid gas through the solution. The HCl gas was generated by dropping hydrochloric acid on anhydrous $CaCl_2$. The HBr and HI gasses were generated by dropping hydrobromic acid or hydroiodic acid solution onto powdered phosphorus pentoxide. All gaseous acids were bubbled into the ether solution using a flow of argon, and the product precipitated immediately. Lower yields were obtained for the HBr and HI samples, perhaps due to the unstable nature of the acid in the gas phase. The product was filtered and dried. The neutral compounds were recrystallized from acetonitrile. All halide salts were recrystallized from methanol. Phase purity was verified by powder X-ray diffraction on a Rigaku Ultima IV instrument with a 2θ ranging from 5° to 65° at a rate of 1° per minute using CuKα radiation. All yields, melting points, and powder X-ray diffractograms may be found in the Supporting Information.

^{1}H solid-state NMR spectroscopy

All ^{1}H SSNMR experiments were performed in a magnetic field of 21.1 T using a Bruker 2.5 mm HX probe and a Bruker Avance II spectrometer. A rotor synchronized Hahn echo ($\pi/2$—τ—π—acq) was used in all cases, with a $\pi/2$ pulse of 2.5 μs. A MAS rate of 31.25 kHz was used for the chloride and bromide samples, whereas in the cases of the iodide samples, a spinning speed of 20 kHz was used. A recycle delay of 360 s was used in all cases, and 8 transients were acquired.

^{13}C solid-state NMR spectroscopy

All ^{13}C CP/MAS SSNMR experiments were performed in a magnetic field of 9.4 T ($\nu_L(^{13}C) = 100.6$ MHz) using a Bruker 4 mm HXY probe and a Bruker Avance III NMR spectrometer. $^{1}H \rightarrow {}^{13}C$ CP was used with a 4.6 μs proton $\pi/2$ pulse, a 2000 μs contact time, and a 54.3 kHz ^{1}H decoupling frequency. ^{13}C chemical shifts were referenced to glycine at 176.6 ppm (^{13}C=O) relative to tetramethylsilane (TMS). Variable spinning speeds were used to separate the spinning sidebands from the isotropic peaks, whereas in the cases of the iodide salts, slower spinning speeds were used to prevent sample decomposition. Further information, such as spinning speeds and the number of scans may be found in Table S2.

^{35}Cl solid-state NMR spectroscopy

Static ^{35}Cl SSNMR spectroscopy was performed in a magnetic field of 21.1 T on a Bruker Avance II NMR spectrometer, using a home-built probe with a 4 mm coil. A quadrupolar echo sequence was used ($\pi/2$—τ—$\pi/2$—acq) was used with a 3 μs $\pi/2$ pulse and a 66 μs echo delay. A total of 2048 transients were collected for 2-IEP·HCl, and 3072 transients were collected for 3-IEP·HCl. MAS experiments were performed using a Bruker 2.5 mm probe, spinning at 31.25 kHz, and using a rotor synchronized quadrupolar echo. A total of 20480 transients were collected for 2-IEP·HCl and 18432 transients were collected for 3-IEP·HCl. In all cases, a recycle delay of 3 s was used. All ^{35}Cl NMR spectra are referenced to NaCl(s) at −41.11 ppm.[83] The static ^{35}Cl spectra were fit using QUEST,[86] whereas the ^{35}Cl MAS spectra were fit with WSolids.[72] The Euler angles follow the passive ZYZ convention,[84] specified within QUEST[86] and WSOLIDS.[72]

$^{79/81}$Br solid-state NMR spectroscopy

Static ^{79}Br and ^{81}Br SSNMR was performed at 21.1 T on a Bruker Avance II NMR spectrometer, using a homebuilt probe with a 5 mm coil. The ^{81}Br acquisition was performed using a quadrupolar echo sequence ($\pi/2-\tau-\pi/2-$acq) with a 0.5 μs $\pi/2$ pulse and a 28.5 μs echo delay with continuous wave proton decoupling, and using a variable-offset cumulative spectral (VOCS)[85] acquisition method with offset changes of $+/-500$ kHz and 24576 transients. All ^{81}Br spectra were processed, and then coadded in the frequency domain to yield the full spectrum. All $^{79/81}$Br spectra were fit using QUEST.[86] The ^{79}Br acquisitions were performed using WURST-QCPMG,[87] with 10 μs pulse lengths, 2 MHz pulse bandwidth sweep from low to high frequency, acquiring 64 echoes with a 10 kHz spikelet separation (8 μs pulse ringdown, 70 μs echo time), and continuous wave proton decoupling. For both compounds, variable-offset cumulative spectral (VOCS)[85] acquisition method was used with offset changes of $+/-500$ kHz with a total of 2048 transients per spectrum. A total of five subspectra were acquired for each sample, processed, and then coadded in the frequency domain to yield the full spectrum. In all cases, a recycle delay of 0.5 s was used. The ^{79}Br and ^{81}Br spectra were referenced to KBr(s) at 54.31 ppm and 54.51 ppm, respectively.[83] The Euler angles follow the passive ZYZ convention,[84] specified within QUEST[86] and WSOLIDS.[72]

Computational details

All DFT and NLMO calculations were performed using the Amsterdam Density Functional software (ADF, 2016)[89–91] using the revised GGA exchange-correlation functional (revPBE) of Zhang and Yang.[92] Models for each compound were generated using GaussView, with atomic positions taken from the crystal structure. The models of 2-IEP·HCl, 2-IEP·HBr, 3-IEP·HBr, and 3-IEP·HI consisted of charged dimers. A theoretical model of the 2-IEP·HI dimer was built using the atomic coordinates from the 2-IEP·HBr dimer. In the case of 2-IEP, 3-IEP, 3-IEP·HCl, and 2-IEP·HI_3, the models included the halogen bond moiety and all interacting molecules. The geometry optimizations were performed using ADF, accounting for relativistic effects (ZORA) and dispersion forces using Grimme3 BJDAMP.[93] All compounds were optimized using the TZP basis set, with the exception of 2-IEP·HBr and the theoretical model of 2-IEP·HI, which were optimized using the TZ2P basis set. The geometry optimization of 2-IEP was performed using only two molecules from the trimer, whereas the geometry optimization of 3-IEP·HCl was performed using the atomic coordinates from 3-IEP·HBr due to convergence difficulties. All NMR calculations were performed using experimental Cartesian coordinates and subsequently on geometry optimized structures. The magnetic shielding tensor and EFG tensor calculations were performed using the TZ2P basis set. Scalar and spin-orbit relativistic effects were accounted for using the zeroth-order regular approximation (ZORA).[94] ^{1}H and ^{13}C calculated shielding constants were converted to chemical shifts using σ_{ref} values of 26.293 ppm[95] and 184.1 ppm,[96] respectively. EFG-Shield was used to extract the EFG tensor orientations.[84]

X-ray crystallography

Crystals of 2-IEP·HCl, 2-IEP·HBr, 2-IEP·HI_3, 3-IEP, 3-IEP·HCl, 3-IEP·HBr, and 3-IEP·HI were mounted on thin glass fibres using paraffin oil. Prior to data collection, the crystals were cooled to 200(2) K. The data were collected on Bruker AXS single-crystal diffractometer equipped with a sealed Mo tube (wavelength 0.71073 Å) and APEX II CCD detector. The raw data collection and reduction were done with the Bruker APEX II software package.[97] Semi-empirical absorption corrections based on equivalent reflections were applied with TWINABS[98] to 2-IEP·HI_3 (twinned data) and SADABS[99] for other datasets. Systematic absences in the diffraction dataset and unit cell parameters were consistent with triclinic $P\bar{1}$ (#2) space group for 3-IEP·HBr, 3-IEP·HI, 2-IEP·HBr, 2-IEP·HCl, monoclinic $P2/c$ (#13) for 3-IEP·HCl, monoclinic $P2_1/c$ (#14) for 2-IEP·HI_3, and orthorhombic *Pbcn* (#60) for 3-IEP. The structures were solved by direct methods and refined with full-matrix least-squares procedures based on F2, using SHELXL[100] and WinGX.[101] All non-H atoms were refined anisotropically. The hydrogen atoms bonded to the nitrogen (H(1) in 3-IEP·HCl, H(1) in 3-IEP·HBr, H(1) in 3-IEP·HI, H(1A) in 2-IEP·HBr, H(1A) in 2-IEP·HCl) were located in the difference Fourier map, while the remaining hydrogen atoms were placed at idealized positions. An exception was 2-IEP·HI_3 where the H(1) atom had to be refined as riding on a corresponding N(1) atom, because of the hydrogen atom's low 50 % occupancy. DFIX restraint was applied to N–H bond distances in 3-IEP·HCl, 3-IEP·HI, 2-IEP·HBr, 2-IEP·HCl. The isotropic displacement parameters U_{iso} of the hydrogen atoms were constrained at 1.2 Ueq of the "parent" N atoms in 3-IEP·HCl, 3-IEP·HI, 2-IEP·HI_3; they were refined freely in 3-IEP·HBr, 2-IEP·HBr, 2-IEP·HCl. Displacement ellipsoid plots were produced using ORTEP,[102] and uncertainties were estimated using PLATON.[103] CCDC 11827955–1827961, contain the supplementary crystallographic data for this paper. These data are provided free of charge by The Cambridge Crystallographic Data Centre.

Acknowledgements

P.M.J.S. and D.L.B. thank the Natural Sciences and Engineering Research Council of Canada for research funding. Access to the 21.1 T NMR spectrometer was provided by the National Ultra-high-Field NMR Facility for Solids (Ottawa, Canada), a national research facility funded by a consortium of Canadian Universities, supported by the National Research Council Canada and Bruker BioSpin, and managed by the University of Ottawa (http://nmr900.ca).

Conflict of interest

The authors declare no conflict of interest.

Keywords: crystal engineering · crystallography · halogen bonding · hydrogen bonding · solid-state NMR

[1] The Nobel Prize in Chemistry **1969**. https://www.nobelprize.org/nobel_prizes/chemistry/laureates/1969/ (accessed July 20th, **2017**).
[2] The Nobel Prize in Chemistry **1987**. https://www.nobelprize.org/nobel_prizes/chemistry/laureates/1987/ (accessed 20 July, **2017**).
[3] G. R. Desiraju, *Crystal Engineering: The Design of Organic Solids*, Elsevier, **1989**.
[4] E. Arunan, G. R. Desiraju, R. A. Klein, J. Sadlej, S. Scheiner, I. Alkorta, D. C. Clary, R. H. Crabtree, J. J. Dannenberg, P. Hobza, H. G. Kjaergaard, A. C. Legon, B. Mennucci, D. J. Nesbitt, *Pure. Appl. Chem.* **2011**, *83*, 1619–1636.
[5] M. H. Kolár, P. Hobza, *Chem. Rev.* **2016**, *116*, 5155–5187.
[6] P. Politzer, J. S. Murray, T. Clark, *Top. Curr. Chem.* **2015**, *358*, 19–42.
[7] H. Wang, W. Wang, W. J. Jin, *Chem. Rev.* **2016**, *116*, 5072–5104.
[8] A. Bauzá, T. J. Mooibroek, A. Frontera, *Angew. Chem. Int. Ed.* **2013**, *52*, 12317–12321; *Angew. Chem.* **2013**, *125*, 12543–12547.

[9] S. Zahn, R. Frank, E. Hey-Hawkins, B. Kirchner, *Chem. Eur. J.* **2011**, *17*, 6034 – 6038.
[10] W. Wang, B. Ji, Y. Zhang, *J. Phys. Chem. A* **2009**, *113*, 8132 – 8135.
[11] F. F. Awwadi, R. D. Willett, K. A. Peterson, B. Twamley, *Chem. Eur. J.* **2006**, *12*, 8952 – 8960.
[12] G. Cavallo, P. Metrangolo, T. Pilati, G. Resnati, G. Terraneo, *Cryst. Growth Des.* **2014**, *14*, 2697 – 2702.
[13] A. C. Legon, *Phys. Chem. Chem. Phys.* **2017**, *19*, 14884 – 14896.
[14] G. Cavallo, P. Metrangolo, R. Milani, T. Pilati, A. Priimagi, G. Resnati, G. Terraneo, *Chem. Rev.* **2016**, *116*, 2478 – 2601.
[15] L. C. Gilday, S. W. Robinson, T. A. Barendt, M. J. Langton, B. R. Mullaney, P. D. Beer, *Chem. Rev.* **2015**, *115*, 7118 – 7195.
[16] T. Clark, M. Hennemann, J. S. Murray, P. Politzer, *J. Mol. Model.* **2007**, *13*, 291 – 296.
[17] G. R. Desiraju, P. Shing Ho, L. Kloo, A. C. Legon, R. Marquardt, P. Metrangolo, P. Politzer, G. Resnati, K. Rissanen, *Pure Appl. Chem.* **2013**, *85*, 1711 – 1713.
[18] P. Metrangolo, H. Neukirch, T. Pilati, G. Resnati, *Acc. Chem. Res.* **2005**, *38*, 386 – 395.
[19] M. Saccone, G. Cavallo, P. Metrangolo, A. Pace, I. Pibiri, T. Pilati, G. Resnati, G. Terraneo, *CrystEngComm* **2013**, *15*, 3102 – 3105.
[20] S. M. Huber, J. D. Scanlon, E. Jimenez-Izal, J. M. Ugalde, I. Infante, *Phys. Chem. Chem. Phys.* **2013**, *15*, 10350 – 10357.
[21] P. Politzer, J. S. Murray, T. Clark, *Phys. Chem. Chem. Phys.* **2010**, *12*, 7748 – 7757.
[22] A. Bondi, *J. Phys. Chem.* **1964**, *68*, 441 – 451.
[23] K. E. Riley, J. S. Murray, J. Fanfrlík, J. Řezáč, R. J. Solá, M. C. Concha, F. M. Ramos, P. Politzer, *J. Mol. Model.* **2011**, *17*, 3309 – 3318.
[24] K. E. Riley, J. S. Murray, J. Fanfrlík, J. Řezáč, R. J. Solá, M. C. Concha, F. M. Ramos, P. Politzer, *J. Mol. Model.* **2013**, *19*, 4651 – 4659.
[25] L. González, N. Gimeno, R. M. Tejedor, V. Polo, M. Blanca Ros, S. Uriel, J. L. Serrano, *Chem. Mater.* **2013**, *25*, 4503 – 4510.
[26] J. Lieffrig, O. Jeannin, M. Fourmigué, *J. Am. Chem. Soc.* **2013**, *135*, 6200 – 6210.
[27] C. B. Aakeröy, T. K. Wijethunga, J. Desper, *J. Mol. Struct.* **2014**, *1072*, 20 – 27.
[28] T. A. Logothetis, F. Meyer, P. Metrangolo, T. Pilati, G. Resnati, *New J. Chem.* **2004**, *28*, 760 – 763.
[29] P. C. Vioglio, M. R. Chierotti, R. Gobetto, *CrystEngComm* **2016**, *18*, 9173 – 9184.
[30] P. M. J. Szell, D. L. Bryce, *Modern Magnetic Resonce* **2016**, pp. 1 – 18, New York, Springer.
[31] J. Viger-Gravel, S. Leclerc, I. Korobkov, D. L. Bryce, *CrystEngComm* **2013**, *15*, 3168 – 3177.
[32] P. C. Vioglio, L. Catalano, V. Vasylyeva, C. Nervi, M. R. Chierotti, G. Resnati, R. Gobetto, P. Metrangolo, *Chem. Eur. J.* **2016**, *22*, 16819 – 16828.
[33] K. Bouchmella, S. G. Dutremez, B. Alonso, F. Mauri, C. Gervais, *Cryst. Growth Des.* **2008**, *8*, 3941 – 3950.
[34] J. Viger-Gravel, S. Leclerc, I. Korobkov, D. L. Bryce, *J. Am. Chem. Soc.* **2014**, *136*, 6929 – 6942.
[35] R. J. Attrell, C. M. Widdifield, I. Korobkov, D. L. Bryce, *Cryst. Growth Des.* **2012**, *12*, 1641 – 1653.
[36] C. M. Widdifield, G. Cavallo, G. A. Facey, T. Pilati, J. Lin, P. Metrangolo, G. Resnati, D. L. Bryce, *Chem. Eur. J.* **2013**, *19*, 11949 – 11962.
[37] P. M. J. Szell, D. L. Bryce, *J. Phys. Chem. C* **2016**, *120*, 11121 – 11130.
[38] Y. Xu, J. Viger-Gravel, I. Korobkov, D. L. Bryce, *J. Phys. Chem. C* **2015**, *119*, 27104 – 27117.
[39] M. Weingarth, N. Raouafi, B. Jouvelet, L. Duma, G. Bodenhausen, K. Boujlel, B. Schöllhorn, P. Tekely, *Chem. Commun.* **2008**, 5981 – 5983.
[40] J. Viger-Gravel, J. E. Meyer, I. Korobkov, D. L. Bryce, *CrystEngComm* **2014**, *16*, 7285 – 7297.
[41] C. Lemouchi, C. S. Vogelsberg, L. Zorina, S. Simonov, P. Batail, S. Brown, M. A. Garcia-Garibay, *J. Am. Chem. Soc.* **2011**, *133*, 6371 – 6379.
[42] D. E. Barry, C. S. Hawes, S. Blasco, T. Gunnlaugsson, *Cryst. Growth Des.* **2016**, *16*, 5194 – 5205.
[43] O. Dumele, D. Wu, N. Trapp, N. Goroff, F. Diederich, *Org. Lett.* **2014**, *16*, 4722 – 4725.
[44] W. N. Moss, N. S. Goroff, *J. Org. Chem.* **2005**, *70*, 802 – 808.
[45] M. Fourmigué, *Acta Crystallogr. Sect. B* **2017**, *73*, 138 – 139.
[46] N. S. Goroff, S. M. Curtis, J. A. Webb, F. W. Fowler, J. W. Lauher, *Org. Lett.* **2005**, *7*, 1891 – 1893.
[47] P. D. Rege, O. L. Malkina, N. S. Goroff, *J. Am. Chem. Soc.* **2002**, *124*, 370 – 371.
[48] See reference [25].
[49] M. Baldrighi, G. Cavallo, M. R. Chierotti, R. Gobetto, P. Metrangolo, T. Pilati, G. Resnati, G. Terraneo, *Mol. Pharm.* **2013**, *10*, 1760 – 1772.
[50] P. M. J. Szell, B. Gabidullin, D. L. Bryce, *Acta Crystallogr. Sect. B* **2017**, *73*, 153 – 162.
[51] P. M. J. Szell, J. Dragon, S. Zablotny, S. R. Harrigan, B. Gabidullin, D. L. Bryce, *New J. Chem.* **2018**, *42*, 10493 – 10501.
[52] A. E. Reed, F. Weinhold, *J. Chem. Phys.* **1985**, *83*, 1736 – 1740.
[53] E. D. Glendening, C. R. Landis, F. Weinhold, *WIREs Comput. Mol. Sci.* **2012**, *2*, 1 – 42.
[54] P. M. J. Szell, A. Siiskonen, L. Catalano, G. Cavallo, G. Terraneo, A. Priimagi, D. L. Bryce, P. Metrangolo, *New J. Chem.* **2018**, *42*, 10467 – 10471.
[55] C.-F. Ng, H.-F. Chow, T. C. W. Mak, *Angew. Chem. Int. Ed.* **2018**, *57*, 4986 – 4990; *Angew. Chem.* **2018**, *130*, 5080 – 5084.
[56] F. F. Awwadi, R. D. Willett, K. A. Peterson, B. Twamley, *J. Phys. Chem. A* **2007**, *111*, 2319 – 2328.
[57] A. Wang, R. Wang, I. Kalf, A. Dreier, C. W. Lehmann, U. Englert, *Cryst. Growth Des.* **2017**, *17*, 2357 – 2364.
[58] F. F. Awwadi, R. D. Willet, B. Twamley, *J. Mol. Struct.* **2009**, *918*, 116 – 122.
[59] M. Freytag, P. G. Jones, *Z. Naturforsch. B* **2001**, *56*, 889 – 896.
[60] S. P. Brown, H. W. Spiess, *Chem. Rev.* **2001**, *101*, 4125 – 4155.
[61] A. E. Aliev, K. D. M. Harris, *Struct. Bonding*, Springer-Verlag, Berlin **2004**, *108*.
[62] M. Kaupp, O. L. Malkina, V. G. Malkin, P. Pyykkö, *Chem. Eur. J.* **1998**, *4*, 118 – 126.
[63] P. Pyykkö, A. Görling, N. Rösch, *Mol. Phys.* **1987**, *61*, 195 – 205.
[64] P. Hrobárik, V. Hrobáriková, F. Meier, M. Repiský, S. Komorovský, M. Kaupp, *J. Phys. Chem. A* **2011**, *115*, 5654 – 5659.
[65] P. Garbacz, K. Jackowski, W. Makulski, R. E. Wasylishen, *J. Phys. Chem. A* **2012**, *116*, 11896 – 11904.
[66] A. K. Cheetham, A. P. Wilkinson, *Angew. Chem. Int. Ed. Engl.* **1992**, *31*, 1557 – 1570; *Angew. Chem.* **1992**, *104*, 1594 – 1608.
[67] P. Hodgkinson, C. M. Widdifield, *C&EN Global Enterp.* **2016**, *94*, 30 – 31.
[68] See reference [31].
[69] V. V. Terskikh, S. J. Lang, P. G. Gordon, G. D. Enright, J. A. Ripmeester, *Magn. Reson. Chem.* **2009**, *47*, 398 – 406.
[70] M. Kaupp, O. L. Malkina, V. G. Malkin, *Chem. Phys. Lett.* **1997**, *265*, 55 – 59.
[71] E. A. C. Lucken, *Nuclear Quadrupole Coupling Constants*, London, Academic Press Inc. **1969**.
[72] K. W. Eichele, Solids1 ver. 1.21.3, **2015**, Universität Tübingen.
[73] See reference [62].
[74] P. M. J. Szell, S. A. Gabriel, R. D. D. Gill, S. Y. H. Wan, B. Gabidullin, D. L. Bryce, *Acta Crystallogr. Sect. C* **2017**, *73*, 157 – 167.
[75] P. Pyykkö, *Mol. Phys.* **2001**, *99*, 1617 – 1629.
[76] R. Sternheimer, *Phys. Rev.* **1950**, *80*, 102 – 103.
[77] R. Sternheimer, *Phys. Rev.* **1951**, *84*, 244 – 253.
[78] D. L. Bryce, C. M. Widdifield, R. P. Chapman, R. J. Attrell, *eMagRes.* **2011**, 321 – 348.
[79] L. P. Wolters, F. M. Bickelhaupt, *ChemistryOpen* **2012**, *1*, 96 – 105.
[80] J. Řezáč, A. de la Lande, *Phys. Chem. Chem. Phys.* **2017**, *19*, 791 – 803.
[81] L. A. Santos, E. F. F. da Cunha, T. C. Ramalho, *J. Phys. Chem. A* **2017**, *121*, 2442 – 2451.
[82] K. Rajender Reddy, M. Vankateshwar, C. Uma Maheswari, P. Santhosh Kumar, *Tetrahedron Lett.* **2010**, *51*, 2170 – 2173.
[83] R. P. Chapman, C. M. Widdifield, D. L. Bryce, *Prog. Nucl. Magn. Reson. Spectrosc.* **2009**, *55*, 215 – 237.
[84] S. Adiga, D. Aebi, D. L. Bryce, *Can. J. Chem.* **2007**, *85*, 496 – 505.
[85] D. Massiot, I. Farnan, N. Gautier, D. Trumeau, A. Trokiner, J. P. Coutures, *Solid State Nucl. Magn. Reson.* **1995**, *4*, 241 – 248.
[86] F. A. Perras, C. M. Widdifield, D. L. Bryce, *Solid State Nucl. Magn. Reson.* **2012**, *45 – 46*, 36 – 44.
[87] L. A. O'Dell, R. W. Schurko, *Chem. Phys. Lett.* **2008**, *464*, 97 – 102.
[88] See reference [84].
[89] G. Te Velde, F. M. Bickelhaupt, E. J. Baerends, C. Fonseca Guerra, S. J. A. van Gisbergen, J. G. Snijders, T. Ziegler, *J. Comput. Chem.* **2001**, *22*, 931 – 967.

[90] C. Fonseca Guerra, J. G. Snijders, G. te Velde, E. J. Baerends, *Theor. Chem. Acc.* **1998**, *99*, 391 – 403.
[91] ADF2016, SCM, Theoretical Chemistry, Vrije Universiteit, Amsterdam, The Netherlands, http://www.scm.com.
[92] Y. Zhang, W. Yang, *Phys. Rev. Lett.* **1998**, *80*, 890.
[93] S. Grimme, S. Ehrlich, L. Goerigk, *J. Comput. Chem.* **2011**, *32*, 1456 – 1465.
[94] E. Van Lenthe, E. J. Baerends, *J. Comput. Chem.* **2003**, *24*, 1142 – 1156.
[95] See reference [65].
[96] A. K. Jameson, C. J. Jameson, *Chem. Phys. Lett.* **1987**, *134*, 461 – 466.
[97] Bruker (2012). APEX2. Bruker AXS Inc.; Madison, Wisconsin, USA.
[98] Bruker (2012). TWINABS. Bruker AXS Inc.; Madison, Wisconsin, USA.
[99] Bruker (2003). SADABS. Bruker AXS Inc.; Madison, Wisconsin, USA.
[100] G. M. Sheldrick, *Acta Crystallogr. Sect. C* **2015**, *71*, 3 – 8.
[101] L. J. Farrugia, *J. Appl. Crystallogr.* **1999**, *32*, 837 – 838.
[102] L. J. Farrugia, *J. Appl. Crystallogr.* **2012**, *45*, 849 – 854.
[103] A. L. Spek, *Acta Crystallogr. Sect. D* **2009**, *65*, 148 – 155.

Manuscript received: March 13, 2018
Revised manuscript received: May 1, 2018
Accepted manuscript online: May 31, 2018
Version of record online: July 5, 2018